On Understanding Bandgap Bowing and Optoelectronic Quality in Pb-Sn Alloy Hybrid Perovskites

Journal:	*Journal of Materials Chemistry A*
Manuscript ID	TA-ART-05-2019-005308.R1
Article Type:	Paper
Date Submitted by the Author:	04-Jun-2019
Complete List of Authors:	Rajagopal, Adharsh; University of Washington, Materials Science and Engineering Stoddard, Ryan ; University of Washington Hillhouse, Hugh; University of Washington, Chemical Engineering Jen, Alex; University of Washington, Materials Science and Engineering; University of Washington, Chemistry

On Understanding Bandgap Bowing and Optoelectronic Quality in Pb-Sn Alloy Hybrid Perovskites

Adharsh Rajagopal,[1] *Ryan J. Stoddard,*[2] *Hugh W. Hillhouse,*[2*] *and Alex K.-Y. Jen*[1,3,4*]

[1]Department of Materials Science and Engineering, University of Washington, Seattle, WA, 98195-2120, USA

[2]Department of Chemical Engineering, Molecular Engineering and Sciences Institute, University of Washington, Seattle, WA 98195-1750, USA

[3]Department of Materials Science & Engineering, City University of Hong Kong, Kowloon, Hong Kong

[4]Department of Chemistry, City University of Hong Kong, Kowloon, Hong Kong

[*]Corresponding Author. E-mail: h2@uw.edu, ajen@uw.edu

ABSTRACT:

High quality small-bandgap hybrid perovskites (AMX_3 with M=$Pb_{1-x}Sn_x$) are pivotal for all-perovskite multi-junction photovoltaics. The bandgap of these alloys significantly deviates from the linear interpolation between the bandgaps of $APbI_3$ and $ASnI_3$ for all A-site cations examined thus far. This non-linearity of bandgap with composition is referred to as bandgap bowing. Here, we explore a wide-range of A-site compositions to understand the bandgap bowing and identify the optimal Pb-Sn alloy composition. Optical and structural investigations of different $APb_{1-x}Sn_xI_3$ alloys reveal that the bandgap bowing is correlated to the extent of microstrain in their respective $APbI_3$ compounds. We discover that bandgap bowing in $APb_{1-x}Sn_xI_3$ alloys is primarily due to local structural relaxation effects (changes in bond angles and lengths) that result from the size, shape, and charge distribution of the cations on the A-site, and that these effects are intimately coupled with chemical effects (intermixing of atomic orbitals) that result from changes in the M-site. The choice of X-site also impacts bandgap bowing because of the X-site anions influence on local structural relaxation and chemical effects. Further, we extend these results to provide a general rationale for the origin and modulation of bandgap bowing in HP alloys. Subsequently, using high-throughput combinational spray coating and photoluminescence analysis, we find that ternary combinations of methylammonium (MA), formamidinium (FA), and cesium (Cs) are beneficial to improve the optoelectronic quality of $APb_{1-x}Sn_xI_3$ alloys. The optimal composition, $(MA_{0.24}FA_{0.61}Cs_{0.15})(Pb_{0.35}Sn_{0.65}I_3)I_3$ has a desirable low bandgap (1.23 eV) and high optoelectronic quality (achieving 86% of the detailed balance limit quasi-Fermi level splitting). This study provides valuable insights regarding bandgap evolution in HP alloys and the optimal small-bandgap absorber composition desired for next-generation HP tandems.

KEYWORDS:

Tandem solar cell, open-circuit voltage, small bandgap, lattice strain, cesium based ternary alloys.

INTRODUCTION

Organic-inorganic hybrid perovskite (HP) semiconductors have sparked high levels on interest for their use in photovoltaics, LEDs, and other devices due to their solution processability and their exceptional structure-property-processing-performance attributes.[1–5] The maximum efficiency for single- and multi-junction perovskite solar cells (PVSCs) depend on the bandgap (E_g) and optoelectronic quality of absorber(s).[6,7] The bandgap of typical HPs with the 3-dimensional (AMX_3) perovskite crystal structure can be tuned extensively by changing the chemical composition.[8] Atomic orbitals of divalent metal cations (*M*-s and *M-p*) and halide anions (*X-p*) dominate electronic character of band edges and primarily determine the bandgap. *A*-site monovalent cations (organic or inorganic) influence tilting of $[MX_6]^{4-}$ octahedra and strength of hydrogen bonding in the 3-dimensional framework and indirectly affect the bandgap. Choices of *A*, *M* and *X* sites also alter structural aspects such as lattice size, octahedral distortion, tilting or rotation, and *M*-cation displacement, all of which have profound impact on the bandgap.[8–10] Composition also influences the nature of defect energy levels, phase stability, and homogeneity at nanoscale, all of which have profound impact on the optoelectronic quality.[11–13] Researching perovskite compositional space thus has immense potential for modulating the bandgap as well as improving the optoelectronic quality of HPs.

Methylammonium lead iodide ($MAPbI_3$), a representative HP composition has a bandgap ~1.6 eV. Through alloying at one or more sites without breaking the AMX_3 structure, E_g of HPs have been tuned from 1.2 to 3.2 eV.[8] Common choices for alloying include formamidinium (FA), guanidinium (GA), cesium (Cs) at *A*-site, tin (Sn) at *M*-site, and bromine (Br) and chlorine (Cl) at *X*-site. Bandgaps for three widely employed binary HP alloys [$(MA,FA)PbI_3$, $MA(Pb,Sn)I_3$ and $MAPb(I,Br)_3$] over the entire composition range are shown in **Figure S1a**. It is evident that bandgaps for alloys deviate from simple linear interpolation between end members and show parabolic dependence on the composition. Alloy ($I_{1-x}II_x$) bandgaps can be well defined with a quadratic fit: $E_g(I_{1-x}II_x) = (1-x).E_g(I) + (x).E_g(II) - b.(x).(1-x)$, where b is the bowing parameter that quantifies the magnitude of the non-linear component. Seminal studies on atomic-scale physical and electronic structure of inorganic semiconductor alloys show that the origin and magnitude of bandgap bowing can be decoupled into three physical contributions: (1) "volume deformation potential" effects – due to compression or dilation of alloys compared to end members; (2) "chemical" effect – due to charge redistribution in alloys with intermixing of atomic orbitals at different energies; (3) "structural relaxation" effects – due to changes in bond angles and bond lengths resulting in new local coordination environment for alloys.[14–17] Other factors like clustering or localization of electronic states introduced by impurity atoms at the dilute limit cause very-large composition-dependent non-parabolic E_g bowing that cannot be defined by a quadratic fit.[18–20]

In HPs, deviation of E_g values from the linear behavior (bandgap bowing) is substantial for the Pb-Sn alloy $MA(Pb,Sn)I_3$, much reduced for the I-Br alloy $MAPb(I,Br)_3$, and almost negligible for the MA-FA alloy $(MA,FA)PbI_3$ (**Figure S1b**). In $MA(Pb,Sn)I_3$ alloys, strong bandgap bowing is coupled with observance of lower bandgaps at intermediate alloy compositions relative to end members and is uncharacteristic when compared with other HP alloys. Lower bandgap Pb-Sn HP alloys are of great interest for application in single-junction (ideal E_g ~1.3 – 1.5 eV) and multi-junction (~1.0 – 1.2 eV for small-E_g subcell) PVSCs.

Literature reports based on *ab-initio* electronic structure calculations provide several possible explanations for bandgap bowing in Pb-Sn HP alloys. Im et al.[21] relate the bandgap lowering to composition induced changes in spin-orbit coupling and structural distortion, whereas

Eperon et al.[22] relate it to the short-range ordering of Pb and Sn atoms in mixed compositions. Recently, a theoretical study by Goyal et al.[23] reported that the composition induced changes in spin-orbit coupling, structural distortion, and short-range ordering all have negligible impact on the bandgap non-linearity. The report identifies "chemical" effects (mismatch in energy for atomic orbitals of Pb and Sn atoms that constitute band edges in alloys) as the major contributor for bandgap bowing in HP alloys (**Figure S2**). However, an experimental study by Parrott et al.[12] using temperature-dependent optical absorption and photoluminescence measurements reported that bandgap bowing in mixed Pb-Sn HP alloys strongly depends on the structural phase and that the characteristic parabolic-nature of bandgap bowing is due to structural relaxation effects (composition dependent local changes in bond-angle for alloys). Thus, there is a conflict about the origin of bandgap bowing in Pb-Sn HP alloys. Is it primarily due to chemical effects, structural effects, or some combination of both?

Compositional modifications also influence the material quality of Pb-Sn HP alloys. Previously, we demonstrated that binary *A*-site compositions such as (MA,FA)[24] and (FA,Cs) or (MA,Cs)[25] improve the performance of $A(\mathrm{Pb,Sn})\mathrm{I}_3$ PVSCs. Later, we also demonstrated that *X*-site modification *via* Br-incorporation [$\mathrm{MA(Pb,Sn)(I,Br)}_3$] significantly improved the absorber optoelectronic quality and yielded PVSCs with improved photovoltage (V_oc = 0.89 V) and efficiency (η = 17.6%).[26] Other groups also have found improvement of Pb-Sn PVSCs using a diverse range of *A*-site and *X*-site modifications, often ascribed to improved morphology and processability,[22] alteration of defect chemistry,[12] defect passivation,[27] larger grain size,[28] and higher stability (phase, air, thermal)[22,29]. Optoelectronic properties also change as function of Pb-Sn content, where ~50-75% Sn containing compositions possess the best properties among mixed compositions for a given $A\mathrm{Pb}_{1-x}\mathrm{Sn}_x X_3$ alloy series.[12,26] The current best performing small-E_g PVSC

(E_g = 1.27 eV, V_{oc} = 0.89 V, η = 19%) employs an optimized composition of $(FA_{0.60}MA_{0.40})(Pb_{0.40}Sn_{0.60})(I_{0.94}Br_{0.06})_3$.[27] Expanding the *A*-site composition to ternary formulations [(FA,MA,Cs), (FA,Cs,Rb)] has been effective to improve the performance and reproducibility of 1.5-1.6 eV E_g Pb-based PVSCs;[30,31] ternary *A*-site combinations [(FA,MA,Cs), (FA,GA,Cs)] have also been pivotal to alleviate the halide phase segregation and improve the optoelectronic quality in 1.7-1.9 eV E_g mixed-halide PVSCs[32,33]. Utilization of ternary *A*-site composition is relatively unexplored in small-E_g PVSCs and has potential to improve the optoelectronic quality of Pb-Sn HP alloys.

In this work, we experimentally investigate how *A*-site composition modification influences the bandgap bowing and optoelectronic quality in Pb-Sn HP alloys. The choice of *A*-site species impacts the structure of the octahedral framework due to steric effects (also referred as chemical pressure, a term commonly used in inorganic oxide perovskites[34,35]). In the first part, we study a series of $APb_{1-x}Sn_xI_3$ alloys using different single and binary *A*-site formulations and determine the associated bandgap bowing using optical absorption measurements. Detailed analysis of the x-ray diffraction patterns shows that: (1) *A*-site modification affects the microstrain (static local displacement of atoms from their crystallographic lattice site) due to changes in steric effects, and (2) the bandgap bowing in $APb_{1-x}Sn_xX_3$ alloys increase proportionally with the microstrain in Pb-end members. Subsequent systematic investigations enabled decoupling of local structural relaxation and chemical effects on bandgap bowing. Integrating our experimental results with insights from literature, we discover a rational and general explanation of the origin and modulation of bandgap bowing in HP alloys. In the second part, we utilize high-throughput compositional exploration *via* spray coating and quantitative steady-state photoluminescence analysis to study the impact of ternary *A*-site formulations on the optoelectronic quality (χ =

$\Delta E_\mathrm{F}/V_\mathrm{OC,SQ}$, where ΔE_F is the quasi-fermi level splitting and $V_\mathrm{OC,SQ}$ is the theoretical limit for photovoltage) of $A\mathrm{Pb}_{1-x}\mathrm{Sn}_x\mathrm{I}_3$ alloys. We find that within the $\mathrm{(MA,FA,Cs)Pb}_{1-x}\mathrm{Sn}_x\mathrm{I}_3$ compositional space, certain ternary A-site combinations improve χ up to 86% and are better than single and binary A-site combinations. Based on these investigations, we identify $\mathrm{(MA_{0.24}FA_{0.61}Cs_{0.15})(Pb_{0.35}Sn_{0.65})I_3}$ as the optimal composition with low-E_g and high optoelectronic quality, and has remarkable potential to improve the performance of multi-junction PVSCs.

RESULTS AND DISCUSSION

Optical and Structural Characteristics of $\mathrm{MA(Pb,Sn)I_3}$ alloys: Pb and Sn have similar outer-shell electronic configuration ($ns^2\ np^2$), octahedral coordination geometry, ionic radius (Sn^{2+} smaller than Pb^{2+} by <10%) and facilitate formation of binary metal substitutional alloys ($A\mathrm{Pb}_{1-x}\mathrm{Sn}_x X_3$) with complete miscibility and small lattice distortions. To contextualize the evolution of bandgap in Pb-Sn HP alloys, we start with the investigation of $\mathrm{MAPb}_{1-x}\mathrm{Sn}_x\mathrm{I}_3$ ($0 \leq x \leq 1$). $\mathrm{MAPb}_{1-x}\mathrm{Sn}_x\mathrm{I}_3$ alloys have a bandgap bowing (b) of 0.61 ± 0.03 eV with the E_g minimum located ~ $x = 0.75$ (**Figure 1**). Based on the above mentioned theoretical and experimental investigations on bandgap bowing in Pb-Sn HP alloys,[12,21–23] it is evident that "chemical" effects combined with effects of "volume deformation potential" and "structural relaxations at the atomic scale" contribute to bandgap bowing in HPs, similar to inorganic compound alloys.[17,23,36]

At room temperature, $\mathrm{MAPbI_3}$ and $\mathrm{MASnI_3}$ crystallize in the tetragonal *I4cm* (β-phase) and (pseudo)cubic *P*4*mm* (α-phase) space groups, respectively.[37] As x increases, the lattice size decreases monotonically (as indicated by changes in the average bond length), and a tetragonal to (pseudo)cubic structural transition is observed ~ $x = 0.50$ (**Figure 1**, **S3** and **Table S2**). The phase transition is induced by reduction in out-of-phase tilting of $[MX_6]^{4-}$ octahedra as x increases and is corroborated by the increase in M-I-M tilting angle from ~163.55° (for $MAPbI_3$) to ~177.43° (for $MASnI_3$) (**Figure 1**); this demonstrates less deviation from linearity for M-I-M bonds in Sn-rich alloys.[21,37] Additionally, as x increases, octahedral distortion increases and is corroborated by the decrease in bond length fraction (ratio between the shortest and longest M-I bonds); increase in octahedral distortion has been attributed to the increased stereochemical activity of lone pair on Sn compared to Pb.[21,38,39] Overall, mircrostrain in the lattice (determined from diffraction angle dependent broadening trends in XRD patterns similar to our previous works[33,40]) decreases with increase in x and a minimum is observed ~ $x = 0.75$ (**Figures 1** and **S4**). This can be rationalized by opposing trends of decrease in octahedral tilting and increase in octahedral distortion as x increases, which have a competing influence on the microstrain of $MAPb_{1-x}Sn_xI_3$ alloys (**Figure 1a-b**).[41] Correlation of bandgap and mircrostrain with minimum values attained similarly ~ $x = 0.75$ point out to the pivotal contributions of local structural relaxations / deformations on the bandgap for Pb-Sn HP alloys,[42–46] and agree with the postulation for bandgap bowing provided by Parrott et al.[12]

Modulation of Bandgap Bowing in $A(Pb,Sn)I_3$ Alloys via A-site Modification: Modification of A-site composition alters chemical pressure (steric effects) on the octahedral framework and affects microstrain by influencing the octahedral tilt angle and distortion.[41,46–48] To assess its impact on bandgap bowing, we fabricated series of $APb_{1-x}Sn_xI_3$ films with various combinations of A-site cations and determined their bandgap from the onset of optical absorption (details in **Experimental Section**). Bandgaps for different $APb_{1-x}Sn_xI_3$ alloys [A = Cs, MA, FA, $FA_{0.8}Cs_{0.2}$ (FACs), $MA_{0.8}Cs_{0.2}$ (MACs), $MA_{0.5}FA_{0.5}$ (MAFA), $MA_{0.8}GA_{0.2}$ (MAGA)] are shown in **Figure 2a**. It is evident that for every series of $APb_{1-x}Sn_xI_3$ alloys, variation in E_g as a function of composition (x) can be well-defined by a quadratic fit (**Figure 2a** and **Table S3**). The bandgap bowing is dependent on the choice of A-site and varies considerably, ranging from 0.57 ± 0.06 eV (for $CsPb_{1-x}Sn_xI_3$) to 0.94 ± 0.16 eV (for $MA_{0.8}GA_{0.2}Pb_{1-x}Sn_xI_3$) as shown in **Figure 2b**. The location of minimum E_g (x_{min}) also changes and appears to vary inversely with bowing (**Figure S5**). Integrating this observation together with the earlier discussion on the influence of band offsets imply that by increasing the bandgap bowing and / or staggered nature of band offsets between end members, we can shift the x_{min} towards lower Sn fractions. These results offer essential guidelines for realization of lower bandgaps with smaller levels of Sn incorporation, which is desired from stability perspective.[49]

A-site modification affects the bandgap of Sn-end members, $ASnI_3$ ($x = 1$) to different extent compared to Pb-end members, $APbI_3$ ($x = 0$) (**Figure 2a**). This is due to structural dissimilarities between $[PbI_6]^{4-}$ and $[SnI_6]^{4-}$ octahedral framework arising from inherent differences in the chemical nature of Pb and Sn. In $APbX_3$, second order Jahn-Teller steric effect (tilts stabilize orbital hybridizations) along with hydrogen bonding between organic A-cation and halide framework facilitate octahedral tilting.[46,48] Whereas in $ASnX_3$, the weakened inert pair effect and increased stereochemically activity of lone pair on Sn[38,39,50] reduces the propensity for octahedral tilting and orbital hybridizations are stabilized by Jahn-Teller octahedral distortion.[48,51,52] These effects explain the above discussed structural deformation trends in $MAPb_{1-x}Sn_xI_3$, where octahedral tilting and octahedral distortion is maximum for $MAPbI_3$ and $MASnI_3$ respectively (**Figure 1**).[21,37] Altogether, the effect on bandgap via A-site modification is primarily modulated by variations in octahedral tilting (changes in linearity of M-X-M bonds) for Pb-perovskites and by volumetric effects (changes in lattice size / microstrain) for Sn-perovskites.[51] Bandgaps of intermediate alloy compositions in $APb_{1-x}Sn_xI_3$ accordingly change based on how a given A-site impacts structural deformation of end members. The interplay between steric effects and strength of hydrogen bonding, which governs the resultant octahedral tilting in intermediate alloy compositions, changes significantly with *A*-site modification[46,48,53] and hence the strong dependence of bandgap bowing on *A*-site for Pb-Sn HP alloys.

For further understanding and obtaining a more comprehensive picture encompassing both *A*-site and *X*-site modifications influence on bandgap bowing, we additionally analyze the bandgaps of $MAPb_{1-x}Sn_xBr_3$ alloys. They have a relatively smaller bandgap bowing parameter (b) of 0.49 ± 0.13 eV with the E_g minimum located ~ $x = 0.70$ (**Figure S6a** and **Table S3**). The significant increase in bandgaps for $MAPb_{1-x}Sn_xBr_3$ alloys compared to $MAPb_{1-x}SnI_3$ alloys can be attributed to the increase in electronegativity of the halide; more strongly bound Br-*p* atomic orbitals lead to upshift of CBM and downshift of VBM in bromine containing compositions relative to their iodine counterparts and hence contain larger bandgaps (**Figure S2**).[54,55] We subsequently performed structural characterization of Pb-end members to get additional insight regarding the bandgap bowing trend in series of $APb_{1-x}Sn_xX_3$ alloys; $FAPbI_3$ and $CsPbI_3$ were omitted due to the difficulty in data acquisition because of the associated phase instabilities.[56] One-dimensional X-ray diffraction (XRD) measurements (standard $\theta/2\theta$ XRD scans with a 1D detector) of powder samples were performed to determine crystal structure, lattice parameters and mircrostrain of Pb-end members (details in **Experimental Section**).

Figures S6b-c show XRD scans for all samples and the associated crystal structure and lattice parameters are listed in **Table S4**. The higher symmetry ((pseudo)cubic crystal structure) in $MAPbBr_3$ and $MA_{0.5}FA_{0.5}PbI_3$ can be rationalized by steric considerations (relative ionic sizes that decrease tilting of octahedra).[57,58] Lattice parameters obtained confirm the trend in lattice size predicted from relative sizes of *A*- and *X*-site ions: $MAPbBr_3 < MA_{0.8}Cs_{0.2}PbI_3 < MAPbI_3 <$

$MA_{0.5}FA_{0.5}PbI_3$ < $FA_{0.8}Cs_{0.2}PbI_3$ < $MA_{0.8}GA_{0.2}PbI_3$. Analysis of microstrain and corresponding values are summarized in **Figure S7**. $MAPbBr_3$ has the lowest microstrain and the amount of microstrain increases with increase in effective size of the *A*-site for $APbI_3$. This trend clearly reflects the impact of increasing chemical pressure on the octahedral framework *via* compositional modification. The above results reveal that the bowing (*b*) in $APb_{1-x}SnxX_3$ alloys are directly correlated with the extent of microstrain (ε) in the $APbX_3$ end members. A plot of *b* versus ε shows linear correlation with a high Pearson correlation coefficient ($r \sim 0.87$) (**Figure 3**). Mechanistically this implies that as the microstrain in Pb-end member increases, local structural relaxation effect changes bandgap to a greater extent with increase in Sn fraction (*x*) and causes a larger deviation in alloy bandgaps from linear interpolation, which transpires as larger bandgap bowing (*b*) for the Pb-Sn alloy series under consideration.

Figure 3 also shows that in the extreme case of zero microstrain, the bandgap bowing intercept in $APb_{1-x}SnxX_3$ alloys is non-zero (~0.3 eV). This indicates the existence of a secondary factor which is independent of *A*-site composition but influences the bowing in $APb_{1-x}Sn_xX_3$ alloys with a given magnitude. Integrating this observation with results from the theoretical study by Goyal et al.[23] that demonstrates the importance of "chemical" effects on bandgap bowing, it is evident that the secondary factor is the mismatch in energy for the atomic orbitals of Pb and Sn atoms that constitute the band edges in alloys (chemical effect), which provides an added contribution to bowing in in $APb_{1-x}SnxX_3$ alloys. Thus, local structural relaxations and chemical effects collectively mediate the bandgap evolution and resultant bowing characteristics in $APb_{1-x}SnxX_3$ alloys.

To evaluate the applicability of this concept for other binary HP alloys, we considered bandgap bowing in I-Br alloys. Bandgap values for series of $MAM(I_{1-y}Br_y)_3$ alloys (M = Pb,

$Pb_{0.75}Sn_{0.25}$, Sn and $0 \leq y \leq 1$) were obtained from literature (**Figure S8a**).[57,59,60] Decrease in bandgap bowing from 0.26 ± 0.03 for $MAPb(I_{1-y}Br_y)_3$ to 0.11 ± 0.05 for $MASn(I_{1-y}Br_y)_3$ correlates well with the decrease in microstrain from $MAPbI_3$ to $MASnI_3$ end members; a plot of bowing in $MAM(I_{1-y}Br_y)_3$ alloys versus microstrain in $MAMI_3$ end members show linear correlation with Pearson's $r \sim 0.99$ (**Figure S8b** and **Table S5**). The reduced bandgap bowing intercept in **Figure S8b** indicates less profound contribution from chemical effect on bandgap bowing in $MAM(I_{1-y}Br_y)_3$ alloys, as rationalized in the discussion above (**Figure S2**). We also considered bandgap bowing in reduced-dimensionality (2D) Pb-Sn HP alloys. Bandgap values for three different 2D Pb-Sn alloy series and the associated structural characteristics of end members were obtained from literature (**Table S6** and **Figure S9a**).[61,62] Bandgap bowing increases with increase in octahedral tilting (deviation from linearity for Sn-I-Sn bonds) (**Table S6** and **Figure S9b**). These examples further merit the pivotal role of local structural relaxations on bandgap evolution and generality of their implications in terms of modulating bandgap bowing behavior in HP alloys. Detailed study of the local structure in HP alloys using Pair Distribution Function (PDF) analysis, nanoscale imaging, and computational modelling will be worthwhile, but are beyond the scope of this study.

Compositional Exploration for High Optoelectronic Quality: In pursuit of high efficiency all perovskite tandem solar cells, lowering the bottom cell bandgap will increase the attainable (detailed-balance limit theoretical maximum) two-terminal efficiency. However, the actual efficiency will also depend strongly on the bottom cell optoelectronic quality. Thus, compositional screening of small-E_g HP candidates must include metrics for both bandgap and optoelectronic quality. Here, we employed absolute intensity photoluminescence (AIPL) to quantify the balance between radiative and non-radiative recombination processes in HP films and assess optoelectronic quality.[63,64] We define an optoelectronic quality parameter χ, where χ is the quasi-Fermi level splitting as a percent of the Shockley-Queisser limit ($\Delta E_{\mathrm{F}}/V_{\mathrm{oc,SQ}}$); see **Supporting Information** for discussion of quasi-Fermi level splitting calculations. Further, we employ combinatorial spray coating to prepare composition gradients with a validated dependence of composition on distance along the substrate (see **Figure S10a** and discussion). Finally, using our compositional screening we chose select compositions to further study with spin coated films, which have the same processing as device fabrication[65]. This compositional screening processes is similar to our prior work exploring (FA,GA,Cs) alloys for high bandgap perovskites.[33]

Eight spray coated composition gradients were selected to fully explore the (MA,FA,Cs) composition space, limiting our exploration compositions with Goldschmidt tolerance factor between 0.92 and 1.00. The specific gradients are shown in **Figure 4a** (note that pure $Cs(Pb_{0.35}Sn_{0.65})I_3$ and pure $FA(Pb_{0.35}Sn_{0.65})I_3$ are excluded since their tolerance factor lies outside of desired range). 360 PL spectra were collected along each composition gradient, creating a total dataset of ~3000 spectra each indexed by composition. Example data for a single gradient are presented in **Figures S10b-c**. Response surfaces to interpolate PL peak position and optoelectronic quality χ within this dataset are presented in **Figures 4b** and **4c** respectively. The peak position remains relatively constant across the entire dataset; all spectra have peak position between 1.22 and 1.25 eV. Note that the Sn content at the bandgap minimum varies with *A*-site composition (**Figures 2a** and **S5**) and we only explore 65% Sn in spray coating studies, thus this does not represent the lowest attainable peak position for a particular *A*-site. The optoelectronic results demonstrate the importance of a small Cs content in attaining high optoelectronic quality, with (MA,Cs) and (FA,Cs) both demonstrating higher quality than (MA,FA) alloys. The ternary (MA,FA,Cs) alloys give the highest overall optoelectronic quality, with the maximum occurring at $A = MA_{0.24}FA_{0.61}Cs_{0.15}$, which demonstrates χ = 86% and peak position = 1.23 eV.

We also note that stability is an important consideration when choosing compositions. Substantial evidence suggests that any compositions containing MA are less stable than the MA-free alternatives,[29,66] although it is still unclear if device innovations and encapsulation strategies can overcome these issues. Thus we also explored MA-free (FA,GA,Cs) compositions, and identified certain (FA,GA,Cs) alloys with higher optoelectronic quality than the (FA,Cs) binary alternatives (see **Figure S11**); incorporation of GA also slightly blue shifts the PL peak position. Collectively, our compositional screening results highlight the potential of ternary A-site formulations with Cs to realize small-E_g Pb-Sn HPs with intrinsically higher optoelectronic quality. In the light of recent results from mechanistic studies on understanding impact of composition in HPs (using transmission electron microscopy,[67] nano-x-ray fluorescence,[13] and Kelvin probe force microscopy[68]), we attribute the observed finding to improved homogeneity of composition and electrical response at nanoscale with Cs incorporation. Furthermore, other recent studies have shown that (MA,FA,Cs) A-site formulation in Pb-based mixed-halide compositions [(MA,FA,Cs)(Pb)(I,Br)] is beneficial for increasing the defect tolerance,[32] and the single-crystal alloys remain stable during at least 10,000 h water-oxygen and 1000 h light stability tests[69].

PL results of spin coated films (**Figures 4d-f** and **S12-S13**) confirm the finding that the (MA,FA,Cs) alloys have higher optoelectronic quality than pure MA. Further, we see that 65% Sn yields the highest optoelectronic quality (for both A = MA and A = (MA,FA,Cs)). A comparison of the AIPL spectra for the film with the highest optoelectronic quality and the lowest peak position in (MA,FA,Cs)(Pb,Sn)I_3 compositional space are shown in **Figure 4f**. They demonstrate that to lower the bandgap by 30 meV with the chosen choice of composition, the ΔE_F decreases from 0.84 to 0.76 eV. Typical PL spectra for all spin coated films studied are shown in **Figure S12**. Note that the processing changes between the spray coated and spin coated films result in slightly different

PL metrics (e.g. χ maximum is 86% for spray coated films and 84% for spin coated films). This suggests that processing also has a strong impact on optoelectronic properties, and that χ of at least 86% should be attainable for spin coated (MA,FA,Cs) films with process optimization, and can be further improved by adapting bulk and interfacial defect passivation approaches from our previous demonstrations of small-E_g Pb-Sn PVSCs[65,70].

CONCLUSION

In summary, we have investigated the influence of A-site modification in $A\mathrm{Pb}_{1-x}\mathrm{Sn}_x\mathrm{I}_3$ alloys for understanding the bandgap bowing behavior in HP alloys and identifying the optimal composition with low-E_g and high optoelectronic quality for small-E_g PVSCs. Bandgap bowing in $A\mathrm{Pb}_{1-x}\mathrm{Sn}_x\mathrm{I}_3$ alloys is strongly dependent on the A-site composition. Systematic optical and structural measurements showed that the extent of bandgap bowing in alloy systems are directly correlated with the microstrain in end members and demonstrated the significant role of local structural relaxation effects. We discover a rational and general explanation of the origin and modulation of bandgap bowing in HP alloys. Subsequently, we utilized high-throughput combinatorial spray coating and AIPL measurements to screen the A-site compositional space for $A(\mathrm{Pb}_{0.35}\mathrm{Sn}_{0.65})\mathrm{I}_3$ alloys. Results revealed that the ternary A-site formulations [(FA,MA,Cs) and (FA,GA,Cs)] have superior optoelectronic quality with respect to their single and binary counterparts. We have found $(\mathrm{MA}_{0.24}\mathrm{FA}_{0.61}\mathrm{Cs}_{0.15})(\mathrm{Pb}_{0.35}\mathrm{Sn}_{0.65}\mathrm{I}_3)\mathrm{I}_3$ to be the optimal composition that has low-E_g (1.23 eV) and high optoelectronic quality (χ = 86%). The enhanced intrinsic optoelectronic quality for the identified small-E_g composition provides a promising platform for the development of next-generation HP multi-junction solar cells.

ASSOCIATED CONTENT

Supporting Information

Experimental Section, Tables S1-S6, Figures S1-S14, and Additional Discussion of Spray Coating Results.

AUTHOR INFORMATION

Corresponding Author

*h2@uw.edu, *ajen@uw.edu

Author Contributions

A.R. conceived and coordinated the overall work, fabricated thin films by spin coating, performed UV-vis and XRD studies. R.J.S. performed spray coating and photoluminescence studies. A.R. wrote the paper and R.J.S. contributed to the corresponding sections. All authors discussed results and reviewed the final paper. H.W.H. and A.K.-Y.J. supervised the entire project.

Notes: The authors declare no competing financial interest.

ACKNOWLEDGMENT

This work was supported by the U.S. Department of Energy Solar Energy Technology Office (award No. DE-EE0006710 and DE-EE0008563), National Science Foundation (No. DMR-1608279), the Office of Naval Research (No. N00014-17-1-2260), and the Asian Office of Aerospace R&D (No. FA2386-15-1-4106). A.K.-Y.J. thanks the Boeing-Johnson Foundation for their financial support. This material is based in part upon work supported by the State of Washington through the University of Washington Clean Energy Institute (CEI) and A.R is grateful for CEI Graduate Fellowship. Part of this work was conducted at the Molecular Analysis Facility, a National Nanotechnology Coordinated Infrastructure site at the University of Washington which is supported in part by the National Science Foundation (No. ECC-1542101). Authors thank Liam Bradshaw for assistance in XRD measurements.

REFERENCES

(1) Rajagopal, A.; Yao, K.; Jen, A. K.-Y. *Adv. Mater.* **2018**, *30* (32), 1800455.
(2) Dunlap-Shohl, W. A.; Zhou, Y.; Padture, N. P.; Mitzi, D. B. *Chem. Rev.* **2019**, *119* (5), 3193–3295.
(3) Jung, M.; Ji, S.-G.; Kim, G.; Seok, S. Il. *Chem. Soc. Rev.* **2019**, 10.1039/C8CS00656C.
(4) Veldhuis, S. A.; Boix, P. P.; Yantara, N.; Li, M.; Sum, T. C.; Mathews, N.; Mhaisalkar, S. G. *Adv. Mater.* **2016**, *28* (32), 6804–6834.
(5) García de Arquer, F. P.; Armin, A.; Meredith, P.; Sargent, E. H. *Nat. Rev. Mater.* **2017**, *2* (3), 16100.
(6) Shockley, W.; Queisser, H. J. *J. Appl. Phys.* **1961**, *32* (3), 510–519.
(7) De Vos, A. *J. Phys. D. Appl. Phys.* **1980**, *13* (83946), 839–846.
(8) Xiao, Z.; Zhou, Y.; Hosono, H.; Kamiya, T.; Padture, N. P. *Chem. - A Eur. J.* **2018**, *24* (10), 2305–2316.
(9) Brenner, T. M.; Egger, D. A.; Kronik, L.; Hodes, G.; Cahen, D. *Nat. Rev. Mater.* **2016**, *1* (1), 15007.
(10) Xiao, Z.; Yan, Y. *Adv. Energy Mater.* **2017**, *7* (22), 1701136.
(11) McMeekin, D. P.; Sadoughi, G.; Rehman, W.; Eperon, G. E.; Saliba, M.; Horantner, M. T.; Haghighirad, A.; Sakai, N.; Korte, L.; Rech, B.; Johnston, M. B.; Herz, L. M.; Snaith, H. J. *Science (80-.).* **2016**, *351* (6269), 151–155.
(12) Parrott, E. S.; Green, T.; Milot, R. L.; Johnston, M. B.; Snaith, H. J.; Herz, L. M. *Adv. Funct. Mater.* **2018**, *28* (33), 1802803.
(13) Correa-Baena, J.-P.; Luo, Y.; Brenner, T. M.; Snaider, J.; Sun, S.; Li, X.; Jensen, M. A.; Hartono, N. T. P.; Nienhaus, L.; Wieghold, S.; Poindexter, J. R.; Wang, S.; Meng, Y. S.; Wang, T.; Lai, B.; Holt, M. V; Cai, Z.; Bawendi, M. G.; Huang, L.; Buonassisi, T.; Fenning, D. P. *Science (80-.).* **2019**, *363* (6427), 627–631.
(14) Zunger, A.; Jaffe, J. E. *Phys. Rev. Lett.* **1983**, *51* (8), 662–665.
(15) Magri, R.; Froyen, S.; Zunger, A. *Phys. Rev. B* **1991**, *44* (15), 7947–7964.
(16) Bernard, J. E.; Zunger, A. *Phys. Rev. B* **1987**, *36* (6), 3199–3228.
(17) Schnohr, C. S. *Appl. Phys. Rev.* **2015**, *2* (3), 031304.
(18) Wei, S.-H.; Zunger, A. *Phys. Rev. B* **1991**, *43* (2), 1662–1677.
(19) Mäder, K. A.; Zunger, A. *Phys. Rev. B* **1995**, *51* (16), 10462–10476.
(20) Kent, P. R. C.; Zunger, A. *Phys. Rev. B* **2001**, *64* (11), 115208.
(21) Im, J.; Stoumpos, C. C.; Jin, H.; Freeman, A. J.; Kanatzidis, M. G. *J. Phys. Chem. Lett.* **2015**, *6* (17), 3503–3509.
(22) Eperon, G. E.; Leijtens, T.; Bush, K. A.; Prasanna, R.; Green, T.; Wang, J. T.-W.; McMeekin, D. P.; Volonakis, G.; Milot, R. L.; May, R.; Palmstrom, A.; Slotcavage, D. J.; Belisle, R. A.; Patel, J. B.; Parrott, E. S.; Sutton, R. J.; Ma, W.; Moghadam, F.; Conings, B.; Babayigit, A.; Boyen, H.; Bent, S.; Giustino, F.; Herz, L. M.; Johnston, M. B.; McGehee, M. D.; Snaith, H. J. *Science (80-.).* **2016**, *354* (6314), 861–865.
(23) Goyal, A.; McKechnie, S.; Pashov, D.; Tumas, W.; Schilfgaarde, M. Van; Stevanović, V. *Chem. Mater.* **2018**, *30* (11), 3920–3928.
(24) Yang, Z.; Rajagopal, A.; Chueh, C.; Jo, S. B.; Liu, B.; Zhao, T.; Jen, A. K.-Y. *Adv. Mater.* **2016**, *28* (40), 8990–8997.
(25) Liu, X.; Yang, Z.; Chueh, C.-C.; Rajagopal, A.; Williams, S. T.; Sun, Y.; Jen, A. K.-Y. *J. Mater. Chem. A* **2016**, *4* (46), 17939–17945.
(26) Yang, Z.; Rajagopal, A.; Jen, A. K.-Y. *Adv. Mater.* **2017**, *29* (47), 1704418.
(27) Li, C.; Song, Z.; Zhao, D.; Xiao, C.; Subedi, B.; Shrestha, N.; Junda, M. M.; Wang, C.; Jiang, C.-S.; Al-Jassim, M.; Ellingson, R. J.; Podraza, N. J.; Zhu, K.; Yan, Y. *Adv. Energy Mater.* **2019**, *9* (3), 1803135.
(28) Zhao, D.; Chen, C.; Wang, C.; Junda, M. M.; Song, Z.; Grice, C. R.; Yu, Y.; Li, C.; Subedi, B.; Podraza, N. J.; Zhao, X.; Fang, G.; Xiong, R.; Zhu, K.; Yan, Y. *Nat. Energy* **2018**, *3* (12), 1093–1100.
(29) Leijtens, T.; Prasanna, R.; Bush, K. A.; Eperon, G. E.; Raiford, J. A.; Gold-Parker, A.; Wolf, E. J.; Swifter, S. A.; Boyd, C. C.; Wang, H.-P.; Toney, M. F.; Bent, S. F.; McGehee, M. D. *Sustain. Energy Fuels* **2018**, *2* (11), 2450–2459.
(30) Correa-Baena, J.-P.; Saliba, M.; Buonassisi, T.; Grätzel, M.; Abate, A.; Tress, W.; Hagfeldt, A. *Science (80-.).* **2017**, *358* (6364), 739–744.
(31) Turren-Cruz, S.-H.; Hagfeldt, A.; Saliba, M. *Science (80-.).* **2018**, *362* (6413), 449–453.
(32) Tan, H.; Che, F.; Wei, M.; Zhao, Y.; Saidaminov, M. I.; Todorović, P.; Broberg, D.; Walters, G.; Tan, F.; Zhuang, T.; Sun, B.; Liang, Z.; Yuan, H.; Fron, E.; Kim, J.; Yang, Z.; Voznyy, O.; Asta, M.; Sargent, E. H. *Nat. Commun.* **2018**, *9* (1), 3100.
(33) Stoddard, R. J.; Rajagopal, A.; Palmer, R. L.; Braly, I. L.; Jen, A. K.-Y.; Hillhouse, H. W. *ACS Energy Lett.* **2018**, *3* (6), 1261–1268.

(34) Avdeev, M.; Jang, L.-Y.; Ricciardo, R. A.; Cuthbert, H. L.; Zhang, Z.; Zhou, Q.; Woodward, P. M.; Kennedy, B. J. *Chem. Mater.* **2010**, *22* (11), 3369–3382.

(35) Morrow, R.; Yan, J.; McGuire, M. A.; Freeland, J. W.; Haskel, D.; Woodward, P. M. *Phys. Rev. B* **2015**, *92* (9), 094435.

(36) Lee, S.; Levi, R. D.; Qu, W.; Lee, S. C.; Randall, C. A. *J. Appl. Phys.* **2010**, *107* (2), 023523.

(37) Hao, F.; Stoumpos, C. C.; Chang, R. P. H.; Kanatzidis, M. G. *J. Am. Chem. Soc.* **2014**, *136* (22), 8094–8099.

(38) Korshunova, K.; Winterfeld, L.; Beenken, W. J. D.; Runge, E. *Phys. status solidi* **2016**, *253* (10), 1907–1915.

(39) Fabini, D. H.; Laurita, G.; Bechtel, J. S.; Stoumpos, C. C.; Evans, H. A.; Kontos, A. G.; Raptis, Y. S.; Falaras, P.; Van der Ven, A.; Kanatzidis, M. G.; Seshadri, R. *J. Am. Chem. Soc.* **2016**, *138* (36), 11820–11832.

(40) Rajagopal, A.; Stoddard, R. J.; Jo, S. B.; Hillhouse, H. W.; Jen, A. K.-Y. *Nano Lett.* **2018**, *18* (6), 3985–3993.

(41) Thomas, N. W. *Acta Crystallogr. Sect. B Struct. Sci.* **1996**, *52* (6), 954–960.

(42) Grote, C.; Berger, R. F. *J. Phys. Chem. C* **2015**, *119* (40), 22832–22837.

(43) Jung, Y. K.; Lee, J. H.; Walsh, A.; Soon, A. *Chem. Mater.* **2017**, *29* (7), 3181–3188.

(44) Yang, R. X.; Skelton, J. M.; Da Silva, E. L.; Frost, J. M.; Walsh, A. *J. Phys. Chem. Lett.* **2017**, *8* (19), 4720–4726.

(45) Bechtel, J. S.; Van der Ven, A. *Phys. Rev. Mater.* **2018**, *2* (2), 025401.

(46) Ghosh, D.; Smith, A. R.; Walker, A. B.; Islam, M. S. *Chem. Mater.* **2018**, *30* (15), 5194–5204.

(47) Filip, M. R.; Eperon, G. E.; Snaith, H. J.; Giustino, F. *Nat. Commun.* **2014**, *5* (1), 5757.

(48) Lee, J.-H.; Bristowe, N. C.; Lee, J. H.; Lee, S.-H.; Bristowe, P. D.; Cheetham, A. K.; Jang, H. M. *Chem. Mater.* **2016**, *28* (12), 4259–4266.

(49) Leijtens, T.; Prasanna, R.; Gold-Parker, A.; Toney, M. F.; McGehee, M. D. *ACS Energy Lett.* **2017**, *2* (9), 2159–2165.

(50) Abrahams, I.; Demetriou, D. Z. *J. Solid State Chem.* **2000**, *149* (1), 28–32.

(51) Prasanna, R.; Gold-Parker, A.; Leijtens, T.; Conings, B.; Babayigit, A.; Boyen, H.-G.; Toney, M. F.; McGehee, M. D. *J. Am. Chem. Soc.* **2017**, *139* (32), 11117–11124.

(52) Tilley, R. J. D. *Perovskites: Structure–Property Relationships*; John Wiley & Sons, Ltd: Chichester, UK, 2016.

(53) Amat, A.; Mosconi, E.; Ronca, E.; Quarti, C.; Umari, P.; Nazeeruddin, M. K.; Grätzel, M.; De Angelis, F. *Nano Lett.* **2014**, *14* (6), 3608–3616.

(54) Castelli, I. E.; García-Lastra, J. M.; Thygesen, K. S.; Jacobsen, K. W. *APL Mater.* **2014**, *2* (8), 081514.

(55) Butler, K. T.; Frost, J. M.; Walsh, A. *Mater. Horiz.* **2015**, *2* (2), 228–231.

(56) Li, Z.; Yang, M.; Park, J.-S.; Wei, S.-H.; Berry, J. J.; Zhu, K. *Chem. Mater.* **2016**, *28* (1), 284–292.

(57) Noh, J. H.; Im, S. H.; Heo, J. H.; Mandal, T. N.; Seok, S. Il. *Nano Lett.* **2013**, *13* (4), 1764–1769.

(58) Weber, O. J.; Charles, B.; Weller, M. T. *J. Mater. Chem. A* **2016**, *4* (40), 15375–15382.

(59) Yang, Z.; Rajagopal, A.; Jo, S. B.; Chueh, C.-C.; Williams, S.; Huang, C.-C.; Katahara, J. K.; Hillhouse, H. W.; Jen, A. K.-Y. *Nano Lett.* **2016**, *16* (12), 7739–7747.

(60) Lai, M. L.; Tay, T. Y. S.; Sadhanala, A.; Dutton, S. E.; Li, G.; Friend, R. H.; Tan, Z.-K. *J. Phys. Chem. Lett.* **2016**, *7* (14), 2653–2658.

(61) Mao, L.; Tsai, H.; Nie, W.; Ma, L.; Im, J.; Stoumpos, C. C.; Malliakas, C. D.; Hao, F.; Wasielewski, M. R.; Mohite, A. D.; Kanatzidis, M. G. *Chem. Mater.* **2016**, *28* (21), 7781–7792.

(62) Zimmermann, I.; Aghazada, S.; Nazeeruddin, M. K. *Angew. Chemie Int. Ed.* **2019**, *58* (4), 1072–1076.

(63) Katahara, J. K.; Hillhouse, H. W. *J. Appl. Phys.* **2014**, *173504*.

(64) Braly, I. L.; Stoddard, R. J.; Rajagopal, A.; Jen, A. K.-Y.; Hillhouse, H. W. *J. Phys. Chem. Lett.* **2018**, *9* (13), 3779–3792.

(65) Rajagopal, A.; Yang, Z.; Jo, S. B.; Braly, I. L.; Liang, P.-W.; Hillhouse, H. W.; Jen, A. K.-Y. *Adv. Mater.* **2017**, *29* (34), 1702140.

(66) Chi, D.; Huang, S.; Zhang, M.; Mu, S.; Zhao, Y.; Chen, Y.; You, J. *Adv. Funct. Mater.* **2018**, *28* (51), 1804603.

(67) Zong, Y.; Wang, N.; Zhang, L.; Ju, M.-G.; Zeng, X. C.; Sun, X. W.; Zhou, Y.; Padture, N. P. *Angew. Chemie Int. Ed.* **2017**, *56* (41), 12658–12662.

(68) Tennyson, E. M.; Roose, B.; Garrett, J. L.; Gong, C.; Munday, J. N.; Abate, A.; Leite, M. S. *ACS Nano* **2019**, acsnano.8b07295.

(69) Chen, L.; Tan, Y.-Y.; Chen, Z.-X.; Wang, T.; Hu, S.; Nan, Z.-A.; Xie, L.-Q.; Hui, Y.; Huang, J.-X.; Zhan, C.; Wang, S.-H.; Zhou, J.-Z.; Yan, J.-W.; Mao, B.-W.; Tian, Z. *J. Am. Chem. Soc.* **2019**, *141* (4), 1665–1671.

(70) Rajagopal, A.; Liang, P.-W.; Chueh, C.-C.; Yang, Z.; Jen, A. K.-Y. *ACS Energy Lett.* **2017**, *2* (11), 2531–2539.

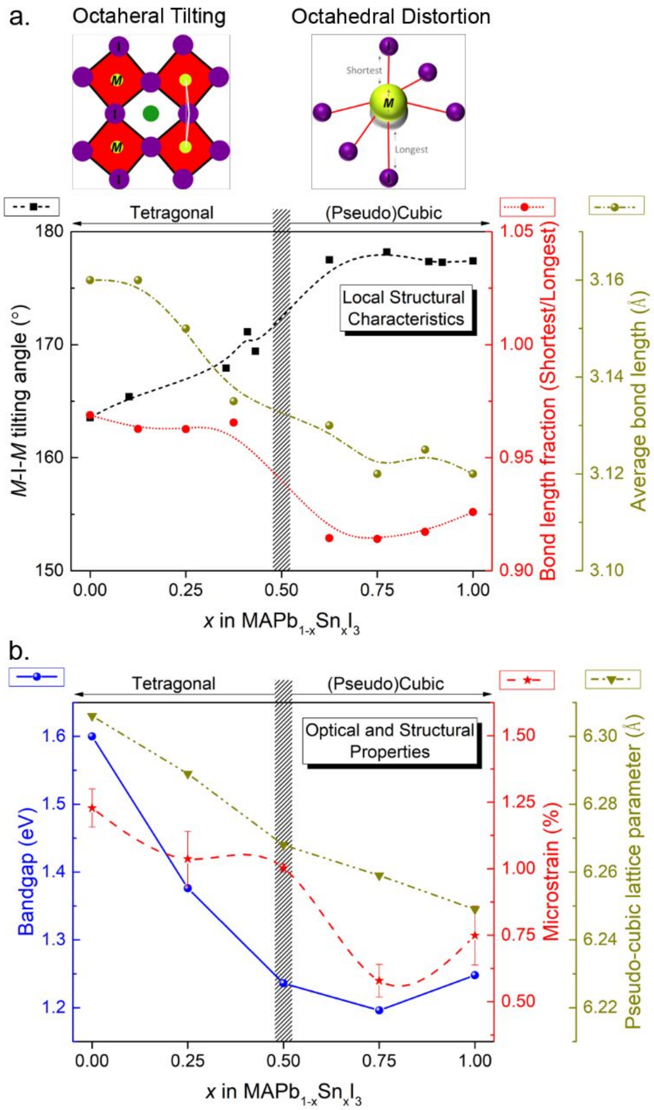

Figure 1. Structural and optical characteristics of $MAPb_{1-x}Sn_xI_3$ alloys. (a) Schematic illustration of octahedral tilting and octahedral distortion. *M*-I-*M* tilting angles, bond length fraction (shortest/longest), and average bond lengths were taken from literature;[21] they respectively provide an indication of octahedral tilting, octahedral distortion, and lattice size in alloy compositions. (b) Bandgaps were determined from the onset of absorption spectra using the 'steepest gradient' method; microstrain and pseudo-cubic lattice parameters were obtained from XRD measurements of powder samples using 1D detector (details in the **Experimental Section**).

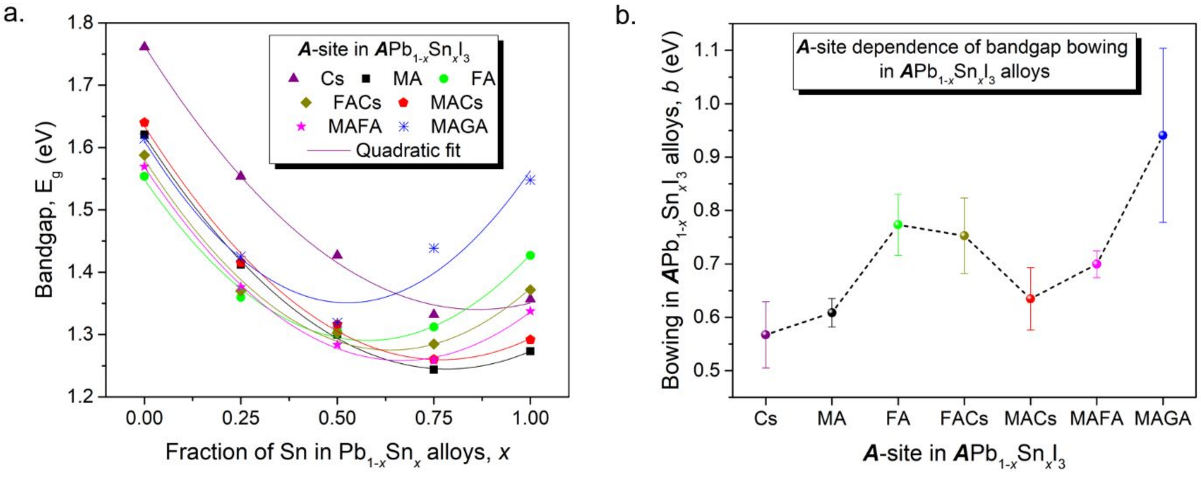

Figure 2. (a) Bandgap variation in *A*Pb$_{1-x}$Sn$_x$I$_3$ alloy compositions ($0 \leq x \leq 1$); bandgap values were determined from the onset of absorption spectra using the 'steepest gradient' method and solid lines represent the quadratic fit of the data (details in the **Experimental Section**). (b) *A*-site dependence of bandgap bowing (*b*) in *A*Pb$_{1-x}$Sn$_x$I$_3$ alloys; dashed lines are provided as a visual aid for observance of changes in *b*.

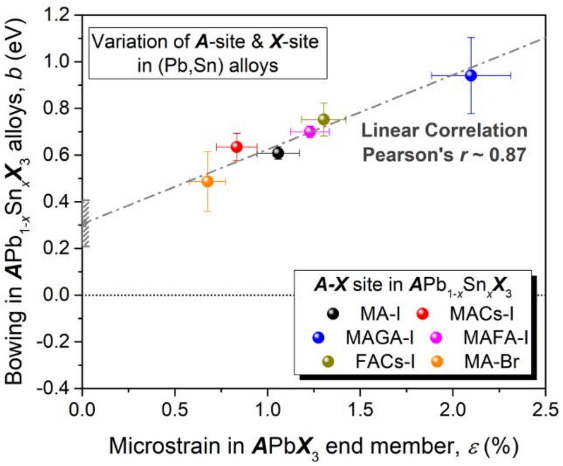

Figure 3. Plot of bandgap bowing in $APb_{1-x}Sn_xX_3$ alloys versus microstrain in their respective $APbX_3$ end members (variation of A-site & X-site in Pb/Sn alloys); a linear correlation with Pearson correlation coefficient (r) ~ 0.87 is observed.

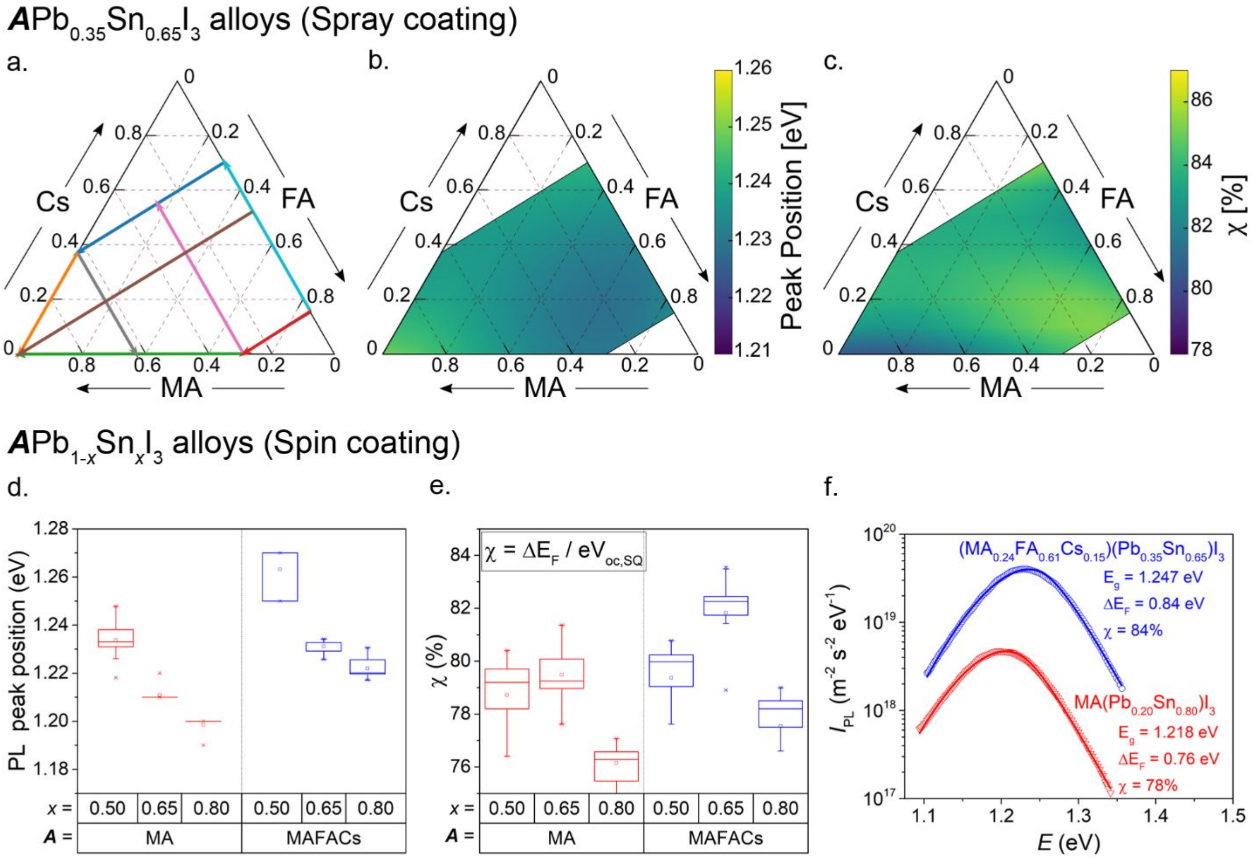

Figure 4. Optoelectronic properties determined from quantitative photoluminescence (PL) measurements on spray coated (a-c) and spin coated (d-f) films. (a) Ternary plot demonstrating the eight gradients included in the (MA,FA,Cs) compositional exploration (each color represents one gradient). The triangle vertices correspond to pure *A* alloys, the edges correspond to two-component alloys, and interior represents ternary (MA,FA,Cs) alloys (65% Sn for all spray coated compositions) (b) PL peak position and (c) optoelectronic quality χ, where χ is the quasi-Fermi level splitting as a percent of the Shockley-Queisser limit, calculated with the PLQY method. (d) PL peak position and (e) optoelectronic quality χ for select spin coated films (statistics from 25 PL spectra collected throughout the film), calculated with the PLQY method. (f) Absolute Intensity PL spectra for [$(MA_{0.24}FA_{0.61}Cs_{0.15})(Pb_{0.35}Sn_{0.65})I_3$] - the spin coated film with the highest optoelectronic quality and [$(MA)(Pb_{0.20}Sn_{0.30})I_3$] - the spin coated film with the lowest peak position compared with a fit to a full peak photoluminescence model.[63] The full peak fit gives the most realistic quasi-Fermi level splitting value since this method accounts for bandgap differences from PL peak and losses from sub-bandgap absorption. Details on the full peak fit and PLQY methods are discussed in **Supporting Information**. Bandgap values from full peak fit method is blue-shifted (<0.02 eV) compared to values obtained from Tauc plot analysis of absorption spectra (**Figure S13b**).

TABLE OF CONTENTS ENTRY

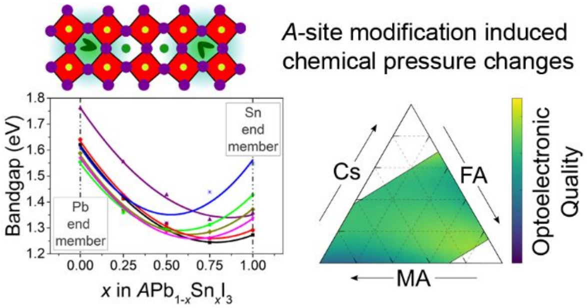

Experimental insights regarding bandgap evolution in hybrid perovskite alloys and the optimal small-bandgap absorber composition desired for next-generation perovskite tandems